Engineering 45 (2025) 52–58

Contents lists available at ScienceDirect

Engineering

journal homepage: www.elsevier.com/locate/eng

Research
Subwavelength Optics—Article

Compound Metalens Enabling Distortion-Free Imaging

Hanyu Zheng [a], Fan Yang [b], Hung-I Lin [a,b], Mikhail Y. Shalaginov [a,b], Zhaoyi Li [a], Padraic Burns [b], Tian Gu [a,b,c,*], Juejun Hu [a,b,c,*]

[a] Department of Materials Science and Engineering, Massachusetts Institute of Technology, Cambridge, MA 02139, USA
[b] 2Pi Inc., Cambridge, MA 02139, USA
[c] Materials Research Laboratory, Massachusetts Institute of Technology, Cambridge, MA 02139, USA

ARTICLE INFO

Article history:
Received 26 March 2024
Revised 27 June 2024
Accepted 10 September 2024
Available online 13 September 2024

Keywords:
Metasurface
Metalens
Wide field of view
Wavefront correction
Compound meta-optics

ABSTRACT

The emergence of metalenses has impacted a wide variety of applications such as beam steering, imaging, depth sensing, and display projection. Optical distortion, an important metric among many optical design specifications, has however rarely been discussed in the context of meta-optics. Here, we present a generic approach for on-demand distortion engineering using compound metalenses. We show that the extra degrees of freedom afforded by a doublet metasurface architecture allow custom-tailored angle-dependent image height relations and hence distortion control while minimizing other monochromatic aberrations. Using this platform, we experimentally demonstrate a compound fisheye metalens with diffraction-limited performance across a wide field of view of 140° and a low barrel distortion of less than 2%, compared with up to 22% distortion in a reference metalens without compensation. The design strategy and compound metalens architecture presented herein are expected to broadly impact metasurface applications in consumer electronics, automotive and robotic sensing, medical imaging, and machine vision systems.

© 2024 THE AUTHORS. Published by Elsevier LTD on behalf of Chinese Academy of Engineering and Higher Education Press Limited Company. This is an open access article under the CC BY-NC-ND license (http://creativecommons.org/licenses/by-nc-nd/4.0/).

1. Introduction

Optical metasurfaces comprising sub-wavelength-scale meta-atoms provide a versatile platform for wavefront control with a compact form factor [1–3]. Major advances in their design, manufacturing, and integration over the past decade have catalyzed the imminent commercial deployment of functional metasurface components in numerous beachhead markets, such as structured light [3–9], computer vision [10–17], near-eye displays [18–24], and beam steering [25–27]. Optical distortion—that is, deviation from rectilinear projection that deforms images—is an important design specification for these applications involving imaging or image/pattern projection. However, while other image-forming attributes of meta-optics, including various other forms of aberrations (i.e., spherical, astigmatism, coma, and chromatic aberrations), have been extensively studied [28–39], distortion and its compensation remain underexplored. Even though distortion, if known and fully mapped, can—on paper—be corrected using post-processing algorithms, this adds computational overhead and degrades the signal-to-noise ratio. For example, radial barrel distortion curtails angular resolution along the tangential/meridional orientation [40]. This problem becomes particularly severe in wide field-of-view (FOV) optical systems [28,41–53] (e.g., fisheye lenses), where large distortion is considered the norm.

In this work, we propose a generic recipe for designing metalenses with on-demand distortion characteristics, which can customize (or arbitrarily define) the relation between the ray angle of incidence (AOI) and the corresponding image height for radially symmetric optics. Unlike a single-layer metalens, whose distortion is fixed, constrained by its aberration minimization condition [54], the extra degrees of freedom afforded by a doublet metalens [28,55–57] enable the concurrent elimination of monochromatic aberrations and the specification of custom-tailored distortion. We experimentally validated our design approach by demonstrating a doublet metalens at a wavelength of 940 nm that simultaneously achieves 140° FOV, diffraction-limited performance, and less than 2% distortion (Fig. 1). In comparison, a singlet metalens without distortion engineering suffers from distortion as high as 22%. The compound metalens design principle, fabrication approach, and characterization results are discussed in the following sections.

* Corresponding authors.
E-mail addresses: gutian@mit.edu (T. Gu), hujuejun@mit.edu (J. Hu).

https://doi.org/10.1016/j.eng.2024.09.004
2095-8099/© 2024 THE AUTHORS. Published by Elsevier LTD on behalf of Chinese Academy of Engineering and Higher Education Press Limited Company.
This is an open access article under the CC BY-NC-ND license (http://creativecommons.org/licenses/by-nc-nd/4.0/).

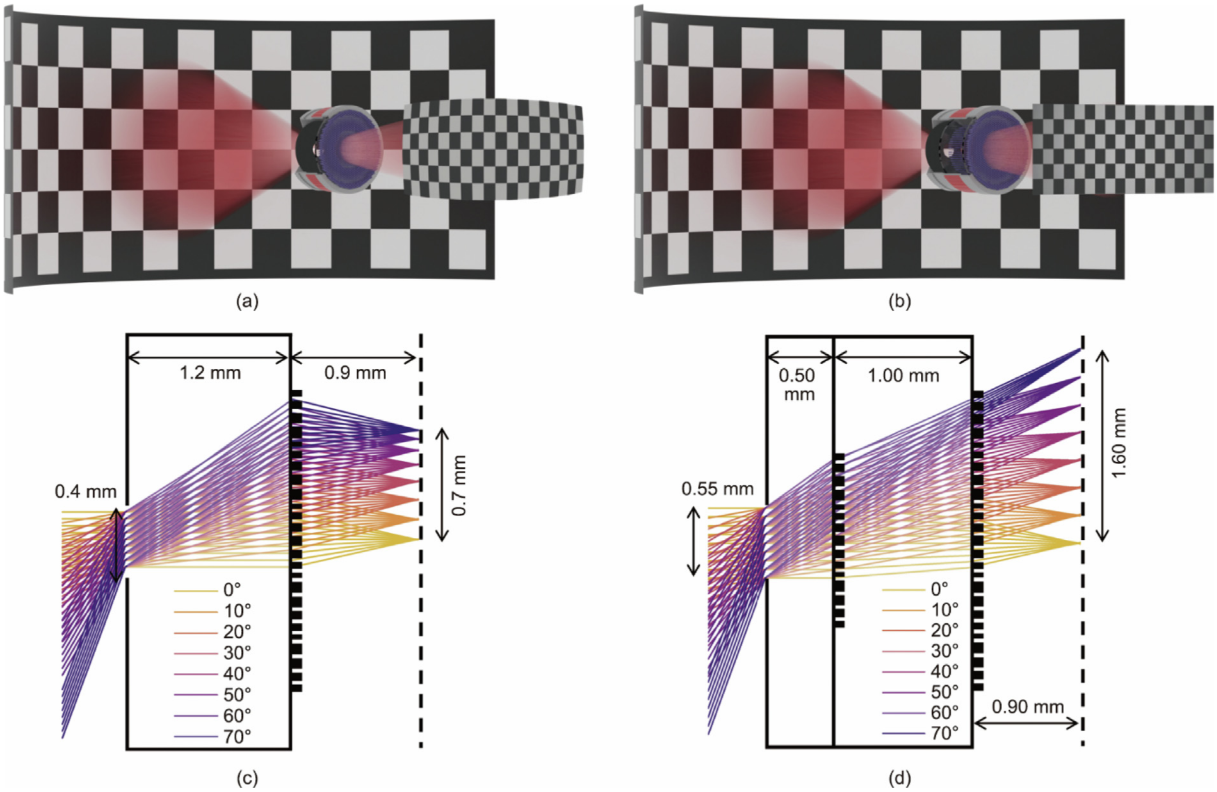

Fig. 1. Comparison of imaging distortion in singlet and compound metalenses. (a) A singlet metalens suffers from large barrel distortion. (b) A compound metalens effectively eliminates the barrel distortion. (c, d) Ray-tracing modeling of the (c) singlet and (d) compound metalens. The light incident angles (in air) vary between 0° and 70° with a step of 10°.

2. Materials and methods

2.1. Numerical simulation

The metasurface comprises amorphous silicon nanopillars with varying diameters on a glass substrate, encapsulated in a uniform polymethyl methacrylate (PMMA) coating. The complex transmission coefficients of the silicon nanopillars were calculated using an open-source rigorous coupled wave analysis (RCWA) solver, Reticolo [58]. A square lattice with a period of 0.32 μm was used for the metasurfaces, with a working wavelength of 0.94 μm. In the simulations, the refractive indices of silicon and PMMA were set at 3.55 and 1.48, respectively, according to the ellipsometry measurement results. The height of the silicon nanopillar was chosen to be 0.74 μm to offer full 2π phase coverage while maintaining high transmission. The meta-atom designs are compiled in Appendix A Section S1.

2.2. Compound metalens design

To ensure and expedite convergence of the metalens optimization process, an analytically derived design was used as the starting input for further numerical fine-tuning using ray tracing on Zemax OpticStudio (ANSYS, Inc., USA). The analytical design uses a predefined image height function as the input and minimizes the aberrations following the stigmatic imaging requirement [54]. The phase gradient of each metasurface was analytically calculated by means of an iterative process, subjected to the constraint that the optical path length (OPL) difference between the neighboring rays approaches zero in the small aperture limit. The detailed derivation process is elaborated in Appendix A Section S2. During the ray trace optimization, the phase profile of each metasurface was defined by even-order polynomials in terms of the radial coordinate ρ, as follows:

$$\phi(\rho) = \sum_{N=1}^{15} a_N \left(\frac{\rho}{R}\right)^{2N} \tag{1}$$

where ϕ is the phase profile of metasurface, N is an integer, R is the normalized radius of the metasurface, and a_N is the optimized coefficient to minimize the focal spot size and maximize the Strehl ratio for AOIs up to 70°. A multi-term error function, $\mathscr{L}$, was defined as follows:

$$\mathscr{L} = \sum u(\alpha) \cdot \mathrm{SZ}(\alpha) + \sum v(\alpha) \cdot |1 - \mathrm{SR}(\alpha)| + \sum w(\alpha) \cdot |S(\alpha) - s(\alpha)| \tag{2}$$

where u, v, and w are the weight of each term, and the summation is performed at AOIs from 0° and 70°. SZ is the focal spot size, SR represents the Strehl ratio, s is the image height, S is the predefined image height function, and α denotes the AOI in air. During the optimization, the function $\mathscr{L}$ is minimized and the size of the front aperture is fixed (for details, see Section S3 in the Appendix A).

2.3. Device fabrication

The metalens field aperture stop was fabricated via laser direct writing. A layer of 10 μm thick black photoresist (Fujifilm, Japan) was spin-coated on a fused silica wafer and pre-baked at 90 °C for 1 min. The photoresist was then exposed to an ultraviolet (UV) laser writer (MLA150, Heidelberg Instruments, Germany), followed by post-baking at 90 °C for 1 min. The sample was then developed in CD-2060 (Fujifilm, Japan) solution for 2 min to complete the aperture stop piece fabrication.

Electron beam lithography (EBL) was used to pattern the metasurfaces. Plasma-enhanced chemical vapor deposition (PECVD) was utilized to deposit a 0.74 μm-thick amorphous silicon device layer on a fused silica substrate. PMMA photoresist was then spin-coated on the silicon layer, followed by baking at a temperature of 180 °C for 2 min and coating a conductive layer of e-spacer (Resonac, Japan). The resist was then exposed in the EBL system (BODEN 150, Elionix, Japan) and developed in a methyl isobutyl ketone/isopropyl alcohol solution. A 30 nm Al_2O_3 hard mask was deposited via electron beam evaporation, followed by a lift-off process with an *N*-methyl-2-pyrrolidone (NMP) solution. The silicon film was then patterned using reactive ion etching (RIE), and a 1 μm-thick layer of PMMA was spin-coated to encase the nanopillar structures as a protective layer.

Lastly, the aperture stop piece was aligned to and bonded with the metasurface substrate to form the final metalens devices. The alignment process was carried out by overlapping the alignment marks on each piece on an automatic die bonder (MRSI M-3, MRSI Systems, Sweden). A UV-cured optical adhesive (NOA 144, Norland Products, Inc., USA) was used as the bonding material. Our bonding process introduces a lateral misalignment of up to 10 μm; however, this has a negligible impact on the device performance, according to our analysis presented in Appendix A Section S4.

3. Results

3.1. Metalens design

Here, we start by examining the design of the reference singlet metalens without distortion compensation. The reference metalens has the same FOV of 140° and assumes the architecture illustrated in Fig. 1(a), which is similar to that of the doublet metalens except that the front metasurface is replaced with an unpatterned aperture. We previously formulated an analytical design framework for such singlet wide-FOV metalenses, which stipulates the following image height function [54]:

$$\mathrm{d}s = \left(\left(\frac{L\cdot\sin\alpha}{\sqrt{n^2-\sin^2(\alpha)}} - s(\alpha)\right)^2 + f^2\right)^{\frac{3}{2}} \cdot \frac{\cos\alpha}{f^2}\mathrm{d}\alpha \tag{3}$$

where L is the spacer thickness, n is the spacer refractive index, ds is the differential image height, and f is the focal length. This condition is derived from aberration minimization in the small-aperture limit and precludes customization of distortion. The sublinear form of image height, $s(\alpha)$, is indicative of barrel distortion, which is commonly seen in wide-FOV optics. The corresponding optical distortion as a function of AOI (D), defined as follows:

$$D = \frac{|s-S|}{S}\cdot 100\% \tag{4}$$

This shows that distortion of up to 22% is present in the singlet metalens system, as discussed in the next section.

Engineering distortion without compromising image quality therefore mandates the introduction of additional design degrees of freedom. We show that a doublet metalens architecture comprising two metasurfaces with an additional entrance field stop in front can fulfill this requirement. As an example, to showcase the on-demand distortion engineering capability, we choose the image height function $S = c\cdot f\cdot\alpha$, where c is a constant. The so-defined image height function completely eliminates distortion in the angular space.

The ray tracing model of the optimized compound metalens is shown in Fig. 1(d), where the index of the layer spacer is set as 1.45. The phase profiles of the metalens are illustrated in Fig. 2(a), including the corresponding phase gradient of each layer, shown in the bottom panel. It is notable that the rays at large AOIs impinge and exit the two metasurfaces, both at oblique angles. This is different from the case of the singlet reference lens, where the rays exit at near-normal angles for all AOIs (i.e., image-space telecentricity). Therefore, the complex coefficient of transmission at various AOIs must be considered. Fig. 2(b) plots the phase delays of the meta-atoms at different AOIs (in air) relative to that of the first meta-atom, and Fig. 2(c) shows the AOI-dependent transmission coefficients of the meta-atoms. The deviation of the phases of the meta-atoms relative to the normal incidence design is presented in Fig. 2(d). The results show minimal phase and transmission variation across the entire 140° FOV. Another source of discrepancy from the meta-atom library design could be caused by deviation from the local phase approximation (LPA), given the large phase gradients near the periphery of the metasurfaces. We therefore simulated the responses of meta-gratings comprising the same set of meta-atoms, which serve as a proxy to assess the impact of non-periodic local environments on metasurface efficiency. The meta-grating efficiencies, averaged over the starting phase [59], are presented in Figs. 2(e) and (f) for different AOIs. Given that the maximum phase gradient in our design is approximately 3 rad·μm^{-1} (denoted as the light shaded area in the figures), the result implies that performance degradation due to deviations from the LPA is insignificant throughout the entire FOV.

3.2. Metalens characterization and distortion-free imaging demonstration

Optical micrographs of the fabricated metasurfaces are shown in Figs. 3(a) and (b). The scanning electron microscopy (SEM) images on the right show the detailed morphology of the metasurfaces in the corresponding region within the black box. Fig. 3(c) shows a photograph of the monolithic metalens assembly after the bonding process. In order to characterize the point-spread function (PSF) of the compound metalens, a customized measurement setup with a rotatable optical axis was built up, as shown in Fig. 4(a). A near-infrared laser at a 0.94 μm wavelength was combined with an 8× beam expander for illumination. The light source was mounted on a rotational stage to offer various AOIs. The PSF of the compound metalens was magnified by 50× through a telescope and captured on a complementary metal-oxide semiconductor (CMOS) imager (1800 U-501m NIR, Allied Vision, Germany). Since the metalens is not telecentric, and the rays are incident on the image plane at oblique angles, the entire imaging part of the setup was mounted onto another rotational stage to match the chief ray direction.

The captured PSFs of the compound metalens at different AOIs are shown in Fig. 4(b). At a larger incident angle, the tangential dimension of the focal spot expands gradually due to an increasing numerical aperture in the non-telecentric lens system. A comparison between measured and ideal (i.e., assuming zero aberration) focal-spot intensity profiles at different AOIs is shown in Fig. 4(c), demonstrating excellent agreement indicative of good fabrication fidelity. In order to quantitatively characterize the focusing quality, the Strehl ratio and modulation transfer function (MTF) curve at each AOI were calculated and compared, as shown in Fig. 4(d). The Strehl ratios consistently stay above 0.8, suggesting a diffraction-limited performance within the entire 140° FOV. The drop in tangential MTF at 70° AOI is a consequence of the increased effective focal length at large AOIs (for more details, see Section S5 in Appendix A).

The optical distortion of the compound metalens was evaluated by directly recording the image height (i.e., focal-spot position) versus AOI, as depicted in Fig. 4(e). The result validates a linear

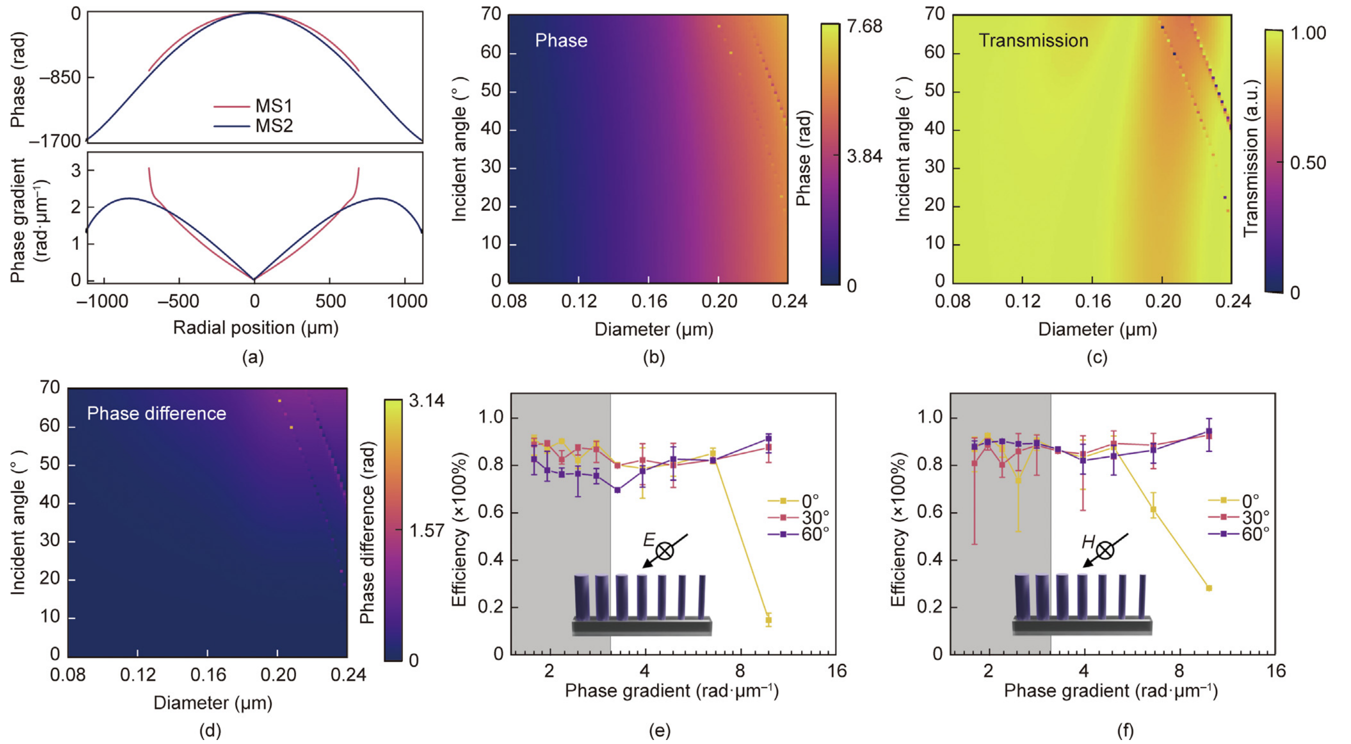

Fig. 2. Compound metalens design. (a) Phase profiles and phase gradients of the compound metalens as functions of the radial position. (b, c) Plots of the (b) angle-dependent phase delay and (c) transmission of the meta-atoms. The diameter of the silicon nanopillars varies between 0.08 and 0.24 μm to obtain 2π phase coverage. (d) Illustration of deviation of the phase delay of the nanopillar meta-atoms from the normal incidence case at different incident angles. (e, f) Simulated meta-grating diffraction efficiencies as functions of the grating phase gradients. The insets depict the simulation configuration. Transverse electric (e) and transverse magnetic (f) polarized light were respectively used as the source with different incident angles. The light shaded areas indicate the phase gradient range used in our compound metalens. MS1: first layer metasurface; MS2: second layer metasurface; *E*: eletric field; *H*: magnetic field.

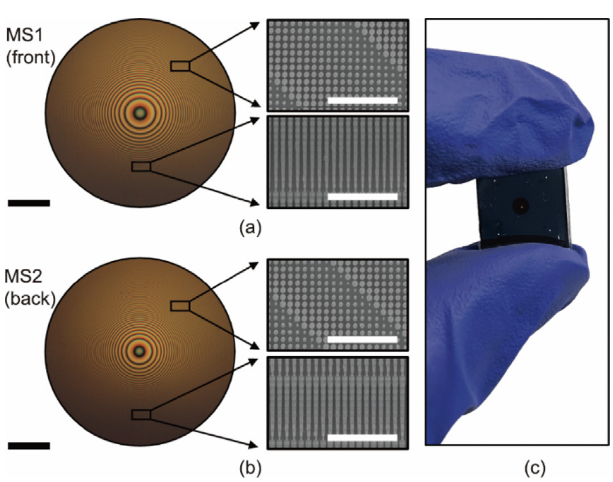

Fig. 3. The fabricated compound metalens. (a, b) Optical images of the partial area in the two metasurfaces. Scale bar: 200 μm. Insets show top- and tilted-view scanning electron microscopy (SEM) images of the meta-atoms. Scale bar: 3 μm. (c) Photo of the assembled compound metalens.

dependence of the image height on the AOI, consistent with our design target. For comparison, the simulated image height of the reference singlet metalens was also plotted. Detailed design specifications of the singlet metalens are provided in Fig. 1(c). The percentage distortions of the two lenses are also compared in Fig. 4(e). The doublet reduces the distortion from up to 22% in the singlet to below 2%—a factor of approximately 10—across the entire viewing field, which is completely negligible for the vast majority of practical applications.

To demonstrate the wide-FOV, distortion-free imaging capability of the compound metalens, a customized imaging setup was built. A cylindrical panoramic target with the printed Massachusetts Institute of Technology (MIT) full name, logo, and an angular scale spanning 180° FOV in the horizontal direction (Fig. 5(a)) sitting on a semicircular three-dimensional (3D)-printed holder was used as the imaging target (for details, see Section S6 in Appendix A). The target was illuminated with a laser torch with a working wavelength of 0.94 μm through an optical diffuser. A commercial off-the-shelf CMOS image sensor (MT9J001, Arducam, China) was used to record the image. Figs. 5(b) and (c) compare the images taken by the (non-distortion-engineered) singlet and (distortion-engineered) compound metalenses. At field angles of over 15°, barrel distortion, which manifests as compression along the radial direction, becomes clear in the image captured by the singlet metalens. This is evident from the inset showing the heavily distorted MIT logo and the compressed scale. In contrast, the barrel distortion is largely absent in the image captured by the compound metalens, evidenced by the evenly distributed angular scale image. The small apparent distortion of the MIT logo along the vertical direction is a result of the cylindrical shape of the target. The radially symmetric compound metalens eliminates distortion in the angular space along both the horizontal and vertical directions; thus, it is designed to map a distortion-free spherical target, rather than a cylindrical one, onto a flat image plane.

4. Discussion

In this paper, we present a generic design principle that enables on-demand distortion engineering for doublet metalenses without

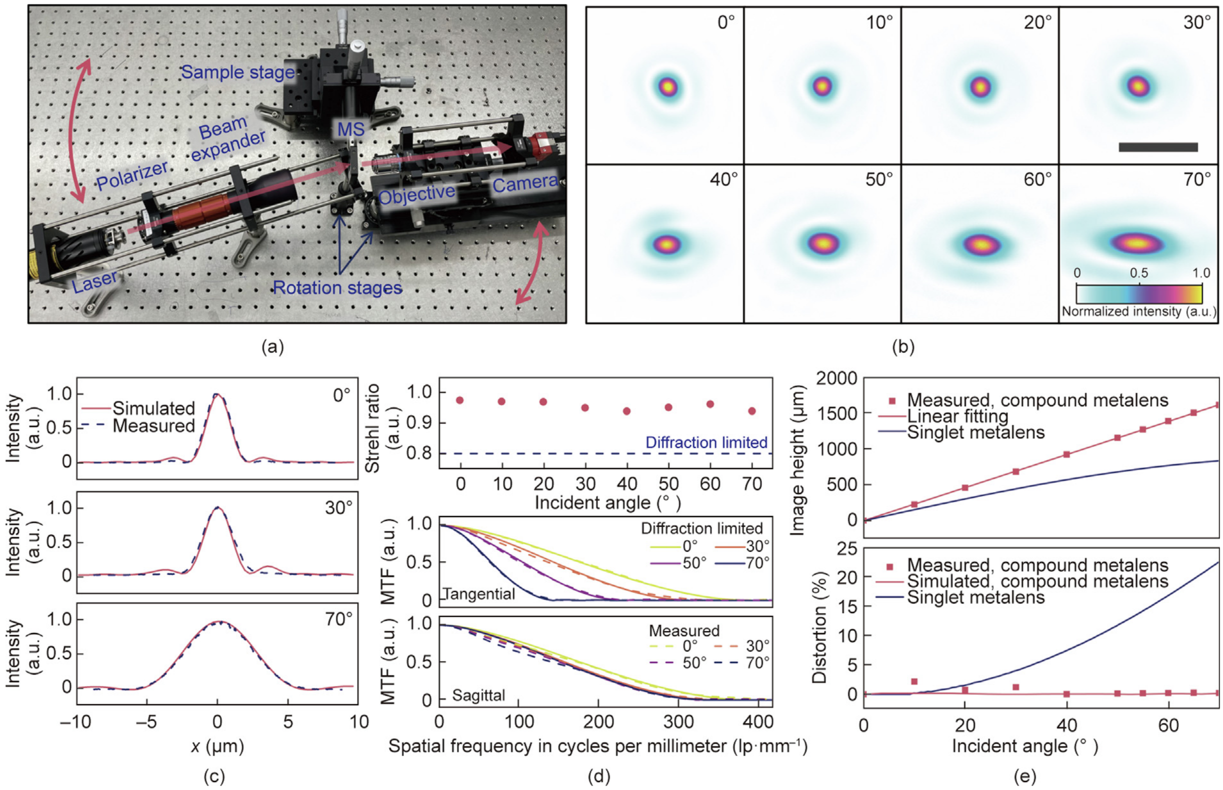

Fig. 4. Optical characterization of the compound metalens. (a) The PSF characterization setup. The light source and imaging system were connected to rotational stages to control the incident angle and the image-capturing direction. (b) The focal spots were captured under different incident angles. Scale bar: 10 µm. (c) Comparison of the measured and simulated focal-spot profiles along the tangential direction at different AOIs. (d) Focusing quality: measured Strehl ratios at different AOIs on the topand measured MTF curves at different incident angles at th bottom. Solid lines: diffraction-limited; dashed lines: measured. (e) Quantitative characterization of image distortion: comparison of the image heights of the compound and singlet metalenses on the topand distortion of the compound and singlet metalenses at the bottom. MS: metasurface; lp·mm^{-1}: line-pair per millimeter.

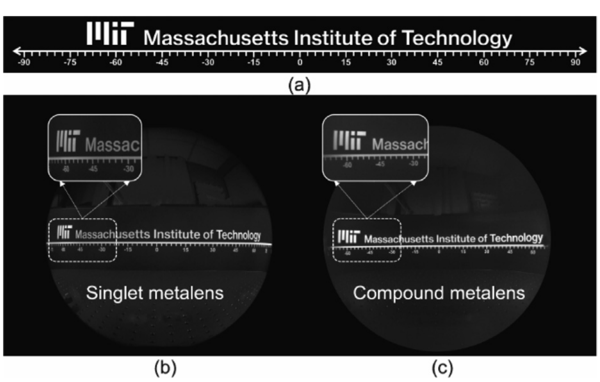

Fig. 5. Imaging test. (a) Design of the printout used as the object, which was mounted on a circular 3D-printed holder. The "MIT" logo and full name are uniformly distributed between ±70° FOV. (b, c) Images taken from the (b) singlet and (c) compound metalenses. The horizontally compressed MIT logo shown in inset (b) is indicative of large barrel distortion.

penalizing their imaging quality. In addition to the linear image height function experimentally demonstrated here, the design can be extended to realize almost arbitrary functional forms of $s(\alpha)$. This is an important new addition to the already-impressive metasurface optics toolbox, allowing designers to meet customers' specifications on lens distortion characteristics. For example, the distortion must be mitigated in projection optics for displays to avoid displayed image distortion and/or loss of resolution. In addition to creating a metasurface "funhouse mirror" at will, the ability to engineer the image height function is critical in suppressing other forms of aberrations, including chromatic aberration. Moreover, the distortion-correction capability is agnostic to the choice of meta-atom types. For example, polarization-sensitive wavefront control can be achieved by means of nanofin structures [60] that can be used for machine vision [10,11], in which polarization multiplexing and distortion-free imaging are essential for feature analysis during optical convolution.

Another useful design variable in our approach is the spacing between the aperture stop, the top, and the bottom metasurfaces, which dictates the chief ray position at each AOI. As an example to showcase the useful designs enabled by this degree of freedom, we present a near-telecentric lens configuration with the distortion fully compensated for (Fig. 6(a)). In this case, the metalens optimization is conducted with the layer thicknesses L_1 and L_2 as variables to constrain the chief ray angle (CRA). The phase functions and gradients are illustrated in Fig. 6(b). The simulated focal spot profiles and distortion across a 120° FOV are displayed in Fig. 6(c), similarly showing zero-distortion behavior in the angular space. The telecentric configuration is useful for integration with CMOS image sensors, since on-sensor microlens arrays or spectral filters typically demand a limited CRA range [61].

5. Conclusions

In summary, we formulated an analytical theory and demonstrated a generic distortion engineering approach that offers on-demand control of the optical distortion characteristics in metalenses. Our approach utilizes a doublet metasurface structure to custom tailor the image height function and CRA without compromising the imaging performance. Applying this principle, we

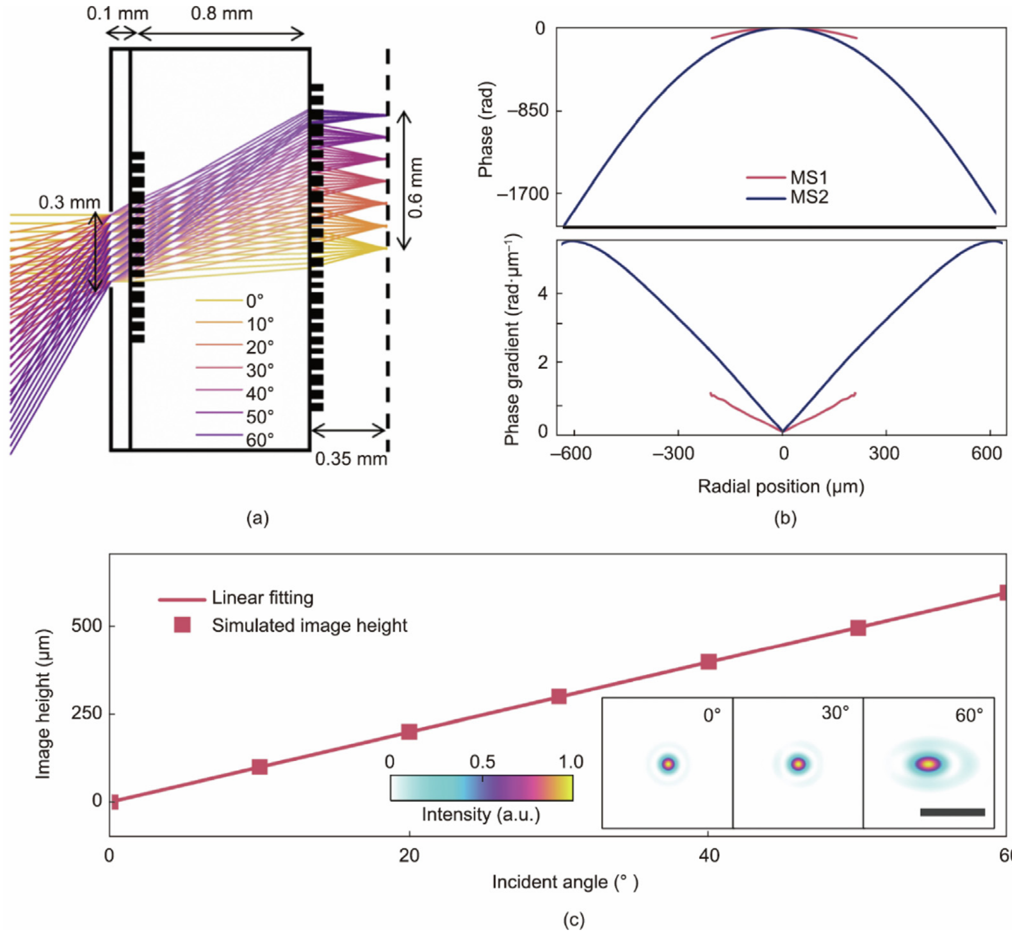

Fig. 6. A distortion-free compound metalens design with a telecentric configuration. (a) Ray-tracing model of the telecentric compound metalens. (b) Phase profiles and phase gradients of the two metasurfaces in the compound metalens. (c) Simulated image height as a function of AOI. Inset shows the simulated PSFs. Scale bar: 10 μm.

experimentally realized a compound metalens concurrently featuring a wide FOV of 140°, diffraction-limited focusing, and distortion-free imaging performance. We further demonstrated that the distortion engineering strategy can be applied to a wide variety of lens configurations and presented the design of a distortion-free telecentric metalens in simulations. The proposed design will find broad applications in next-generation metasurface optics systems for imaging, projection, depth sensing, and machine vision.

Acknowledgments

This work was performed in part at the Center for Nanoscale Systems (CNS), Harvard University and MIT.nano.

Juejun Hu and Tian Gu acknowledge funding support provided by the Defense Advanced Research Projects Agency Defense Sciences Office Program: Enhanced Night Vision in Eyeglass Form (ENVision).

Compliance with ethics guidelines

Hanyu Zheng, Fan Yang, Hung-I Lin, Mikhail Y. Shalaginov, Zhaoyi Li, Padraic Burns, Tian Gu, and Juejun Hu declare that they have no conflict of interest or financial conflicts to disclose.

Appendix A. Supplementary data

Supplementary data to this article can be found online at https://doi.org/10.1016/j.eng.2024.09.004.

References

[1] Yu N, Capasso F. Flat optics with designer metasurfaces. Nat Mater 2014;13(2):139–50.
[2] Kamali SM, Arbabi E, Arbabi A, Faraon A. A review of dielectric optical metasurfaces for wavefront control. Nanophotonics 2018;7(6):1041–68.
[3] Dorrah AH, Capasso F. Tunable structured light with flat optics. Science 1979;2022:376.
[4] Ni Y, Chen S, Wang Y, Tan Q, Xiao S, Yang Y. Metasurface for structured light projection over 120° field of view. Nano Lett 2020;20(9):6719–24.
[5] Kim G, Kim Y, Yun J, Moon SW, Kim S, Kim J, et al. Metasurface-driven full-space structured light for three-dimensional imaging. Nat Commun 2022;13:5920.
[6] Wang QH, Ni PN, Xie YY, Kan Q, Chen PP, Fu P, et al. On-chip generation of structured light based on metasurface optoelectronic integration. Laser Photonics Rev 2021;15(3):2000385.
[7] Hsu WC, Chang CH, Hong YH, Kuo HC, Huang YW. Metasurface- and PCSEL-based structured light for monocular depth perception and facial recognition. Nano Lett 2023;24(5):1808–15.
[8] Li C, Li X, He C, Geng G, Li J, Jing X, et al. Metasurface-based structured light sensing without triangulation. Adv Opt Mater 2024;12(7):2302126.
[9] Deng L, Jin R, Xu Y, Liu Y. Structured light generation using angle-multiplexed metasurfaces. Adv Opt Mater 2023;11(16):2300299.
[10] Zheng H, Liu Q, Zhou Y, Kravchenko II, Huo Y, Valentine J. Meta-optic accelerators for object classifiers. Sci Adv 2022;8(30):eabo6410.
[11] Zheng H, Liu Q, Kravchenko II, Zhang X, Huo Y, Valentine JG. Multichannel meta-imagers for accelerating machine vision. Nat Nanotechnol 2024;19(4):471–8.
[12] Huang AL, Tanguy QAA, Fröch JE, Mukherjee S, Böhringer KF, Majumdar A. Photonic advantage of optical encoders. Nanophotonics 2023;13(7):1191–6.
[13] Swartz BT, Zheng H, Forcherio GT, Valentine J. Broadband and large-aperture metasurface edge encoders for incoherent infrared radiation. Sci Adv 2024;10(6):eadk0024.
[14] Luo X, Hu Y, Ou X, Li X, Lai J, Liu N, et al. Metasurface-enabled on-chip multiplexed diffractive neural networks in the visible. Light Sci Appl 2022;11:158.
[15] Li W, Ma Q, Liu C, Zhang Y, Wu X, Wang J, et al. Intelligent metasurface system for automatic tracking of moving targets and wireless communications based on computer vision. Nat Commun 2023;14:989.

[16] Neshev DN, Miroshnichenko AE. Enabling smart vision with metasurfaces. Nat Photonics 2023;17:26–35.
[17] Li L, Zhao H, Liu C, Li L, Cui TJ. Intelligent metasurfaces: control, communication and computing. eLight 2022;2:7.
[18] Lan S, Zhang X, Taghinejad M, Rodrigues S, Lee KT, Liu Z, et al. Metasurfaces for near-eye augmented reality. ACS Photonics 2019;6(4):864–70.
[19] Lee GY, Hong JY, Hwang SH, Moon S, Kang H, Jeon S, et al. Metasurface eyepiece for augmented reality. Nat Commun 2018;9:4562.
[20] Li Z, Lin P, Huang YW, Park JS, Chen WT, Shi Z, et al. Meta-optics achieves RGB-achromatic focusing for virtual reality. Sci Adv 2021;7(5):eabe4458.
[21] Li Z, Pestourie R, Park JS, Huang YW, Johnson SG, Capasso F. Inverse design enables large-scale high-performance meta-optics reshaping virtual reality. Nat Commun 2022;13:2409.
[22] Song W, Liang X, Li S, Li D, Paniagua-Domínguez R, Lai KH, et al. Large-scale Huygens' metasurfaces for holographic 3D near-eye displays. Laser Photonics Rev 2021;15(9):2000538.
[23] Yang Y, Seong J, Choi M, Park J, Kim G, Kim H, et al. Integrated metasurfaces for re-envisioning a near-future disruptive optical platform. Light Sci Appl 2023;12:152.
[24] Song W, Liang X, Li S, Moitra P, Xu X, Lassalle E, et al. Retinal projection near-eye displays with Huygens' metasurfaces. Adv Opt Mater 2023;11(5):2202348.
[25] Deng Y, Wu C, Meng C, Bozhevolnyi SI, Ding F. Functional metasurface quarter-wave plates for simultaneous polarization conversion and beam steering. ACS Nano 2021;15(11):18532–40.
[26] Tao J, You Q, Li Z, Luo M, Liu Z, Qiu Y, et al. Mass-manufactured beam-steering metasurfaces for high-speed full-duplex optical wireless-broadcasting communications. Adv Mater 2022;34(6):2106080.
[27] Zhang Y, Fowler C, Liang J, Azhar B, Shalaginov MY, Deckoff-Jones S, et al. Electrically reconfigurable non-volatile metasurface using low-loss optical phase-change material. Nat Nanotechnol 2021;16(6):661–6.
[28] Arbabi A, Arbabi E, Kamali SM, Horie Y, Han S, Faraon A. Miniature optical planar camera based on a wide-angle metasurface doublet corrected for monochromatic aberrations. Nat Commun 2016;7:13682.
[29] Shrestha S, Overvig AC, Lu M, Stein A, Yu N. Broadband achromatic dielectric metalenses. Light Sci Appl 2018;7:85.
[30] Wang S, Wu PC, Su VC, Lai YC, Chen MK, Kuo HY, et al. A broadband achromatic metalens in the visible. Nat Nanotechnol 2018;13(3):227–32.
[31] Aiello MD, Backer AS, Sapon AJ, Perreault JD, Llull P, Acosta VM. Achromatic varifocal metalens for the visible spectrum. ACS Photonics 2019;6(10):2432–40.
[32] Fan Z, Qiu HY, Zhang HL, Pang XN, Zhou LD, Liu L, et al. A broadband achromatic metalens array for integral imaging in the visible. Light Sci Appl 2019;8:67.
[33] Arbabi A, Faraon A. Advances in optical metalenses. Nat Photonics 2023;17:16–25.
[34] Engelberg J, Levy U. The advantages of metalenses over diffractive lenses. Nat Commun 2020;11:1991.
[35] Khorasaninejad M, Chen WT, Devlin RC, Oh J, Zhu AY, Capasso F. Metalenses at visible wavelengths: diffraction-limited focusing and subwavelength resolution imaging. Science 1979;2016(352):1190–4.
[36] Chen J, Ye X, Gao S, Chen Y, Zhao Y, Huang C, et al. Planar wide-angle-imaging camera enabled by metalens array. Optica 2022;9(4):431.
[37] Guo Y, Ma X, Pu M, Li X, Zhao Z, Luo X. High-efficiency and wide-angle beam steering based on catenary optical fields in ultrathin metalens. Adv Opt Mater 2018;6(19):1800592.
[38] Zhang F, Pu M, Li X, Ma X, Guo Y, Gao P, et al. Extreme-angle silicon infrared optics enabled by streamlined surfaces. Adv Mater 2021;33(11):2008157.
[39] Martins A, Li J, Borges BHV, Krauss TF, Martins ER. Fundamental limits and design principles of doublet metalenses. Nanophotonics 2022;11(6):1187–94.
[40] Lee M, Kim H, Paik J. Correction of barrel distortion in fisheye lens images using image-based estimation of distortion parameters. IEEE Access 2019;7:45723–33.
[41] Liu W, Li Z, Cheng H, Tang C, Li J, Zhang S, et al. Metasurface enabled wide-angle Fourier lens. Adv Mater 2018;30(23):1706368.
[42] Li S, Hsu CW. Thickness bound for nonlocal wide-field-of-view metalenses. Light Sci Appl 2022;11:338.
[43] Engelberg J, Zhou C, Mazurski N, Bar-David J, Kristensen A, Levy U. Near-IR wide-field-of-view Huygens metalens for outdoor imaging applications. Nanophotonics 2020;9(2):361–70.
[44] Shalaginov MY, An S, Yang F, Su P, Lyzwa D, Agarwal AM, et al. Single-element diffraction-limited fisheye metalens. Nano Lett 2020;20(10):7429–37.
[45] Groever B, Chen WT, Capasso F. Meta-lens doublet in the visible region. Nano Lett 2017;17(8):4902–7.
[46] Arbabi E, Arbabi A, Kamali SM, Horie Y, Faraji-Dana MS, Faraon A. MEMS-tunable dielectric metasurface lens. Nat Commun 2018;9:812.
[47] Xie T, Zhang F, Pu M, Bao H, Jin J, Cai J, et al. Ultrathin, wide-angle, and high-resolution meta-imaging system via rear-position wavevector filter. Laser Photonics Rev 2023;17(9):2300119.
[48] Martins A, Li K, Li J, Liang H, Conteduca D, Borges BHV, et al. On metalenses with arbitrarily wide field of view. ACS Photonics 2020;7(8):2073–9.
[49] Yang F, An S, Shalaginov MY, Zhang H, Rivero-Baleine C, Hu J, et al. Design of broadband and wide-field-of-view metalenses. Opt Lett 2021;46(22):5735.
[50] Lassalle E, Mass TWW, Eschimese D, Baranikov AV, Khaidarov E, Li S, et al. Imaging properties of large field-of-view quadratic metalenses and their applications to fingerprint detection. ACS Photonics 2021;8(5):1457–68.
[51] Yu H, Cen Z, Li X. Achromatic and wide field of view metalens based on the harmonic diffraction and a quadratic phase. Opt Express 2022;30(25):45413.
[52] Fan CY, Lin CP, Su GDJ. Ultrawide-angle and high-efficiency metalens in hexagonal arrangement. Sci Rep 2020;10:15677.
[53] Shalaginov MY, Lin H, Yang F, Weninger DM, Li C, Agarwal AM, et al. Metasurface-enabled wide-angle stereoscopic imaging. In: Proceedings of Frontiers in Optics + Laser Science 2022; 2022 Oct 17–20; Rochester, NY, USA; 2022.
[54] Yang F, An S, Shalaginov MY, Zhang H, Hu J, Gu T. Understanding wide field-of-view flat lenses: an analytical solution. Chin Opt Lett 2023;21(2):023601.
[55] Zheng H, He M, Zhou Y, Kravchenko II, Caldwell JD, Valentine JG. Compound meta-optics for complete and loss-less field control. ACS Nano 2022;16(9):15100–7.
[56] Zhou Y, Kravchenko II, Wang H, Zheng H, Gu G, Valentine J. Multifunctional metaoptics based on bilayer metasurfaces. Light Sci Appl 2019;8:80.
[57] Yang F, Gu T, Hu J. Analytical design framework for metasurface projection optics. J Opt Soc Am B 2023;40(8):2211.
[58] Hugonin AJP, Lalanne P. RETICOLO CODE 1D for the diffraction by stacks of lamellar 1D gratings. 2012. arXiv:2101.00901.
[59] Arbabi A, Arbabi E, Mansouree M, Han S, Kamali SM, Horie Y, et al. Increasing efficiency of high numerical aperture metasurfaces using the grating averaging technique. Sci Rep 2020;10:7124.
[60] Yang F, Lin HI, Shalaginov MY, Stoll K, An S, Rivero-Baleine C, et al. Reconfigurable parfocal zoom metalens. Adv Opt Mater 2022;10(17):2200721.
[61] McClung A, Samudrala S, Torfeh M, Mansouree M, Arbabi A. Snapshot spectral imaging with parallel metasystems. Sci Adv 2020;6(38):eabc7646.